Lasers in Manufacturing and Materials Processing (2021) 8:237–255
https://doi.org/10.1007/s40516-021-00147-1

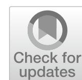

Dry Etching of Germanium with Laser Induced Reactive Micro Plasma

Martin Ehrhardt[1] · Pierre Lorenz[1] · Jens Bauer[1] · Robert Heinke[1] · Mohammad Afaque Hossain[1] · Bing Han[2] · Klaus Zimmer[1]

Accepted: 18 May 2021 / Published online: 16 June 2021
© The Author(s) 2021

Abstract

High-quality, ultra-precise processing of surfaces is of high importance for high-tech industry and requires a good depth control of processing, a low roughness of the machined surface and as little as possible surface and subsurface damage but cannot be realized by laser ablation processes. Contrary, electron/ion beam, plasma processes and dry etching are utilized in microelectronics, optics and photonics. Here, we have demonstrated a laser-induced plasma (LIP) etching of single crystalline germanium by an optically pumped reactive plasma, resulting in high quality etching. A Ti:Sapphire laser ($\lambda = 775$ nm, $E_{Pulse/max.} = 1$ mJ, $t = 150$ fs, $f_{rep.} = 1$ kHz) has been used, after focusing with a 60 mm lens, for igniting a temporary plasma in a CF_4/O_2 gas at near atmospheric pressure. Typical etching rate of approximately ~ 100 nm / min and a surface roughness of less than 11 nm rms were found. The etching results were studied in dependence on laser pulse energy, etching time, and plasma – surface distance. The mechanism of the etching process is expected to be of chemical nature by the formation of volatile products from the chemical reaction of laser plasma activated species with the germanium surface. This proposed laser etching process can provide new processing capabilities of materials for ultra—high precision laser machining of semiconducting materials as can applied for infrared optics machining.

Keywords Plasma formation · Laser · Reactive etching · Ge · CF_4 · Optical breakdown

✉ Martin Ehrhardt
martin.ehrhardt@iom-leipzig.de

✉ Klaus Zimmer
klaus.zimmer@iom-leipzig.de

[1] Leibniz Institute of Surface Engineering (IOM), Permoserstr. 15, 04318 Leipzig, Germany

[2] School of Elec. & Opt. Eng, Nanjing University of Science & Technology, Xiaolingwei 200, Nanjing 210094, China

Introduction

The demands of surface quality increases continuously due to continues miniaturization in microelectronics and the speed of developments in nano- and molecular technologies. The requirement of manipulation of molecules, atoms or light at atomic level stress the requirements of high precision surface machining enabling a platform that bridges molecular level and the interface to daily applications. Traditionally, dry etching of semiconductor materials is an important method for structuring of surface in the micrometer and sub-micrometer range. Examples of dry etching are ion beam bases methods [1, 2] in which the material removal process is dominated by physical sputtering of surface atoms. Dry etching with reactive plasmas is another method. Plasma etching is a dry etching technology performed with electrically pumped plasma excitation that is applied regularly for pattern transfer in microelectronics [3, 4]. In this case, the material removal process is based mainly on a chemical reaction of species generated in the plasma with the surface atoms. The products of this reaction have to be volatile in order to maintain a stable material removal process. The mainly physical based sputter process can be combined with a chemical-based plasma etching process, for instance, reactive-ion etching [3, 5]. However, ion beam or plasma-based processes typically that they require complex equipment, processes and they mostly require to be performed in vacuum condition. Ultra-precise surface machining can be achieved by atmospheric – pressure plasma jets (APPJ). APPJ was investigated in the last decades extensively [6–8]. The footprint of APPJ is typically in the range of mm or sub-mm range. A disadvantage of APPJ processing is that the plasma is not only in contact with the substrate but also with the electrodes, chamber wall as well with the nozzle. This causes for example a corrosion of the nozzle and in consequence contamination of the surface via the plasma. Germanium (Ge) is a material which is widely used in micro-electronics, photovoltaic, and micro-optics. Plasma etching of Ge was investigated extensively and many studied have been published related to Ge etching in various configurations [9–15] using fluorine and chlorine-based processes. In general, both dry etching behavior and characteristics of the etched surface are similar for silicon and germanium due to their similar chemical structure [14–16]. However, details of the etching mechanism differ between Ge and Si and it was found that chemically formed intermediates can interfere the Si etching (SiO_xF_y in the case of Si etching) but do not hinder Ge etching (GeO_xF_y in the case of Ge etching) [9].

Laser ablation processing can also be categorized as a dry etching method which can be performed in non-vacuum condition. Laser micro processing of surfaces is a very flexible process and is widely used in industrial application. Regardless of the many advantages of laser ablation processing, this process is not commonly used for high precise structuring of semiconductor. The reason is that with laser processing high ablation rate of typically 10 to 100 nm/pulse are found [17]. The surface quality in terms of roughness and surface / sub-surface damage are inferior in comparison to e.g. plasma—based processes.

Only a limited number of techniques have been reported which make use of a dry laser structuring processes based on a chemical etching [18–21]. These processes can be classified into two groups. In one group, the surface is directly exposed to laser irradiation. The laser heats the surface in the focal spot and a chemical reaction between the surface and an etching gas is activated due to photothermal processes. In the other group, the wavelength of the laser radiation must match the absorption of the etching gas which is activated by the laser radiation due to e.g. photodissociation. However, both of the laser dry etching processes are limited to a specific I) etching gas, II) laser source and III) material combination. Due to these very specific requirements, these processes are not suitable for broader applications, e.g. microelectronic or optical industry.

A new concept of laser based dry etching was introduced by Elhadj et al. [22]. Elhadj et al. used nanosecond laser radiation in order to generate a plasma by optical break down in N_2 and ambient air. By translating the plasma near a SiO_2 surface, the laser-induced plasma (LIP) could interact with the surface. However, it was reported that the surface was damaged due this laser/plasma interaction. By a glancing angle of irradiation relative to the substrate, a thermal induced material removal due to melting and evaporation was found.

In the present study, a dry etching process based on a laser generated reactive plasma has been investigated. With this concept, the authors have shown that a dry etching of SiO_2 could be achieved using CF_4 as etchant in a previous study [23]. The surface quality of etched areas was high with surface roughness value as low as 1.4 nm rms and etching rate in the range of ~25 nm/s. The ignition of the plasma with every applied laser pulse provides precise control of the etching depth. This characteristic in combination with the etching footprint in sub-millimeter and micrometre range enables the usage of the process in a broad range of applications. Possible application examples are selective modification and trimming of microelectronic elements, optical applications such as the generation of free form optics or correction of optical waviness, and local surface modification for biomedical applications. For the investigation of the Ge etching in the present study, the free-standing reactive plasma has been generated by an optical breakdown in a CF_4/O_2 atmosphere. The laser produced plasmas provide a localized and contamination free processing and, therefore, allow a number of innovative processing schemas, in sharp contrast to electrically pumped plasmas. Here, ultra-short laser pulses ($\lambda = 775$ nm, $t = 150$ fs) have been used to generate the optical breakdown. Then, the resulting plasma has been transferred to the proximity of the surface of a single crystalline germanium <111> without exposing the surface to the laser radiation. At a specific plasma-surface distance, the reactive species of the plasma etch the surface. The dependence of etching characteristics on the laser pulse energy, etch time, plasma – sample distance has been investigated. The morphology of generated etch grooves in the Ge surface has been imaged by SEM and AFM. The surface composition has been analyzed by XPS (X-ray photoelectron spectroscopy), SIMS (Secondary-ion mass spectrometry) and compared with the untreated surface. The obtained results have been summarized and discussed in detail.

Experimental Details

The experimental setup is shown in Fig. 1 that comprises the laser source and the etch chamber, both included in a laser workstation. The laser source provides ultra-short laser pulses with a wavelength (λ) of 775 nm, a pulse duration (t_p) of 150 fs, a pulse repetition rate (f_{rep}) of 1 kHz, and a maximum pulse energy (E_p) of 1 mJ. The laser beam that can be attenuated by polarizing beam splitter is guided by mirrors to the chamber and is focused there into the chamber through an entrance window by a 60 mm focal length lens. If the applied pulse energy exceeds a certain threshold an optical visible plasma is generated due to an optical breakdown. In Fig. 2, an image of the laser-induced plasma generated at typical process parameter is shown. The position and the distance of the plasma has been monitored with two cameras through two additional windows. Hence, the camera system could resolve the plasma position with a precision of ~ 5 µm. The chamber that has been fixed on a computer-controlled X–Y-Z translation stage that can be moved with a resolution of ~ 1 µm enabling the precise control of the relative position of the plasma inside the chamber and in relation to the substrate.

Inside the chamber the samples have been fixed on heater that is hold at a temperature of ~ 473 C° with three clamps. The sample surface has been aligned parallel to the laser beam propagation direction. A gas feed and pressure control unit has been attached to the chamber. The absolute gas pressure has been fixed to a value of 85 ± 5 kPa. CF_4 and O_2 gases have been fed constantly inside the chamber with flow rates of 498 sccm and 330 sccm, respectively. In comparison to chamber sized plasma processes in the case of the present laser – plasma process the chamber volume is with an inner volume of ~ 400 cm^2 much larger compared to the plasma volume (estimated to be much less than 10mm^3) induced by the laser. The sample

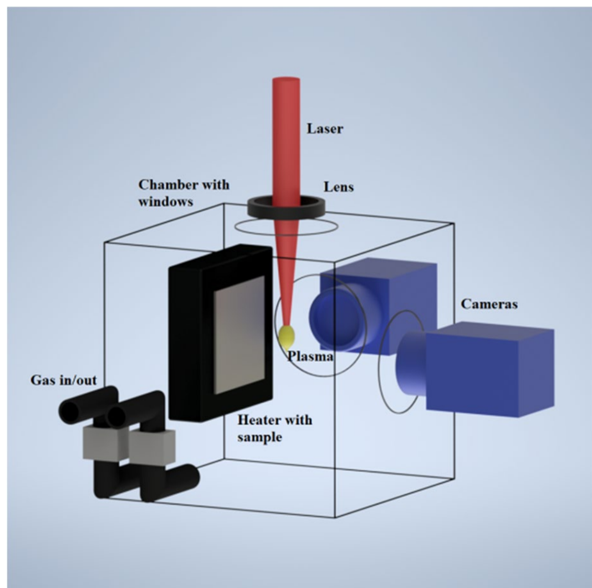

Fig. 1 Sketch of the experimental setup. The LIP can be controlled by cameras positioned near the heated sample surface enabling the etching of the germanium

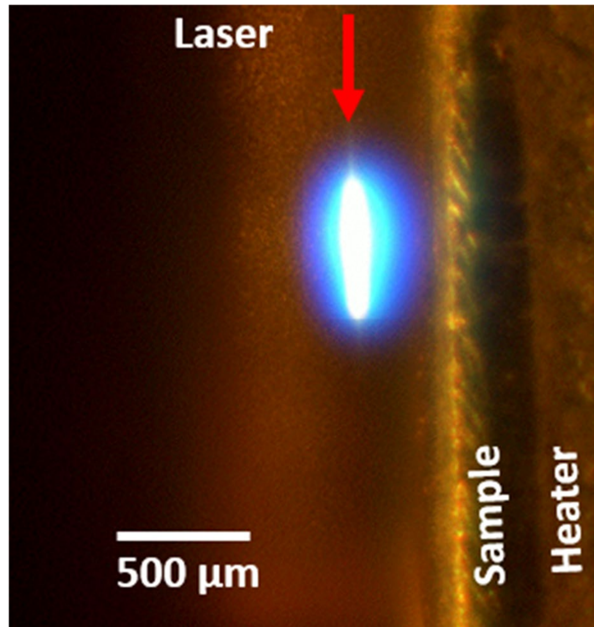

Fig. 2 Image of a typical laser induced plasma (LIP) inside the etching chamber during the etching process. In addition to the plasma the samples surface can be seen

material used is a one side polished single crystalline Ge (CRYSTAL GmbH, Berlin) with a size of 10 × 10 mm and a thickness of 0.5 mm. The crystal orientation of the Ge sample is < 111 > . Before the etching experiments, the sample were cleaned by a two-step process. I) washing in a solution of 1 ml NH_4OH, 2 ml H_2O_2 und 40 ml H_2O and II) ultra-sonic clean at 50 C° in a solution of 1 ml HCl, 2 ml H_2O_2 und 8 ml H_2O for 20 min. Subsequently, the samples were dried by spin-off and heating for 3 min at 115 °C. The samples were stored in a dry atmosphere up to 3 days before they were used for the experiments.

The samples have been imaged by white light interference microscopy (WLIM) (Bruker, NPFLEX) and AFM (Dimension ICON; Bruker) after the etching process.

The WLIM measurements were performed in phase-shift mode using objectives with 5 × and 10 × magnifications and a 1 × field multiplier resulting in image sizes of 1230 µm × 925 µm and 624 µm × 467 µm and an lateral pixel resolution of ~ 2 µm and 1 µm, respectively.

AFM was operated in tapping modeTM in a xy-closed loop configuration. The sample was imaged in a scanning area of 10 µm × 10 µm with a pixel field of 1024 × 1024. The raw data were subjected to a plane correction consisting of a global plane fit and a line-wise correction subtracting a fitted polynomial function of the 3rd order from each scan line via SPIP™ software (version 6.0.14 by Image Metrology). A SEM (Gemini Ultra 55, Zeiss) has been used to image the sample surface using secondary electron imaging mode.

Before imaging the samples with WLIM, AFM and SEM the samples were clean with the same two-step process as it was applied for preparation the samples before the etching process.

The chemical composition of the surface before and after the etching process is explored by X-ray photoelectron spectroscopy (XPS, Kratos Ultra DLD). The measurements are performed at room temperature with a background pressure of 1×10^{-7} Pa. For excitation, monochromic Al Kα radiation at 1486.6 eV is used. The X-ray gun is operated at 150 W. Photoelectrons are released from the 300 µm x 700 µm analysis area and are analysed under normal incidence configuration. The photoelectron yield is enhanced applying a magnetic immersion lens. To avoid sample charging a neutralizer supplies thermal electrons to the analysis area. A retarding lens system coupled by a hemispherical analyser with 40 eV pass energy is used for energy separation. The energy-filtered photoelectrons are amplified passing a microchannel plate and recorded by a delay line detector. The UNIFIT 2021 software is used for spectra analysis and composition calculation considering the specific transmission correction of the XPS machine. For curve fitting convolved Gaussian–Lorentzian peak profiles are simultaneously optimized with a Shirley background profile.

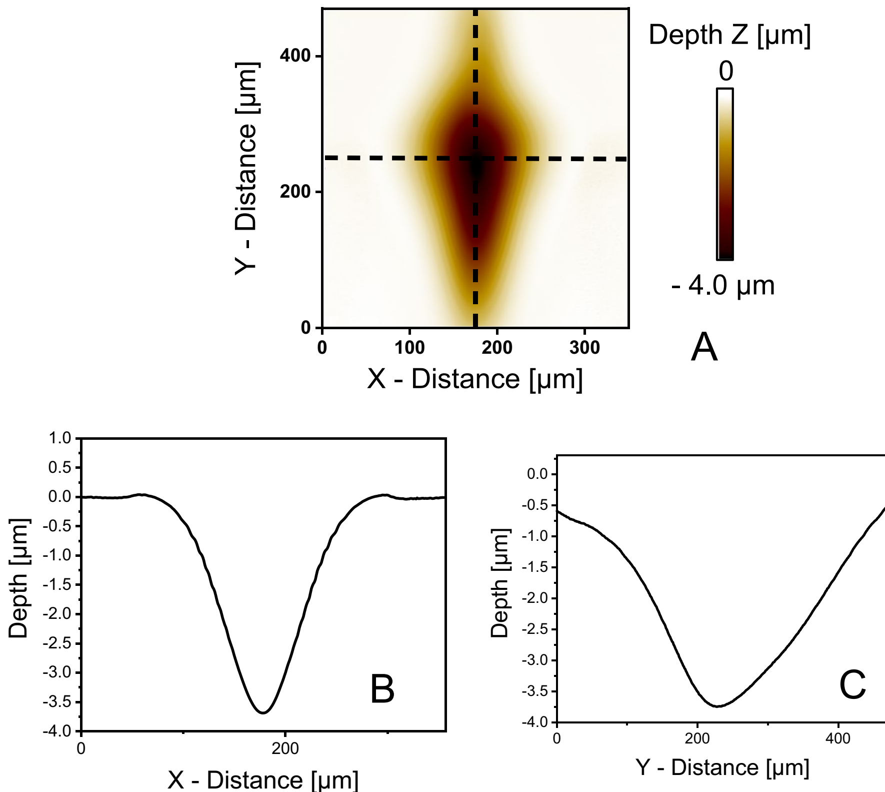

Fig. 3 Contour plot of an exemplary etching groove measured by WLIM. **B** Shows a cross-section of the etching groove along the X-axe, marked in **A** with the dotted line. **C** Shows a cross-section of the etching groove along the Y-axe, marked in **A** with the dotted line. The etch groove was generated with an etching time of 3 min and a pulse energy of ~ 400 µJ

Time-of flight secondary ion mass spectrometry (ToF–SIMS; IONTOF TOF SIMS 5) was used for depth profiling of the sample composition near the surface. Therefore, a 15 keV Ga ion beam scans a field of (50×50) μm^2 that is centred within the (300×300) μm^2 area that is sputtered with a 500 eV caesium ion beam for depth profiling The depth calibration of the analysis is provided by WLIM measurement of the final sputter crater depth.

Initially, a plasma is generated inside the chamber with laser pulses having a pulse energy of 740 μJ to localize the plasma center. Thereafter the sample is moved by the stages in relation to the plasma to set the distance between the plasma center and the sample surface (denoted subsequently as plasma distance).

Results

The plasma distance is fixed to 100 μm for this set of experiments. The plasma distance is defined in the following as the distance between the center of the plasma and the sample surface. Due to the interaction of the plasma with the sample, optical-visible etching grooves are produced. Frist the surface was imaged, and the groove etching depth was measured by WLIM. In Fig. 3 a contour plot as well as cross-sections of an exemplary etching groove can be seen. The etching groove is asymmetric in X and Y direction. Whereas the etching groove is longer in beam propagation direction, which is the Y-axes in Fig. 3a. The dimension of the etching groove does not correlate with the size of the laser focal spot but with the dimension of the laser induced plasma (see Fig. 2).

The time dependence of the depth of the etched grooves is plotted in Fig. 4. The graph shows clearly that the etching depth increases with increasing the etching time. A depth d of 29.5 μm could be achieved for the maximum applied etching time of 15 min. The slope of the depth decreases at higher etching times. In order to quantify this effect instantaneous etching rate is calculated by differentiate the etching depth with the etching time. The calculated instantaneous etching rate has it peak value of ~ 66 nm/ s at an etching time of 120 s. Afterwards

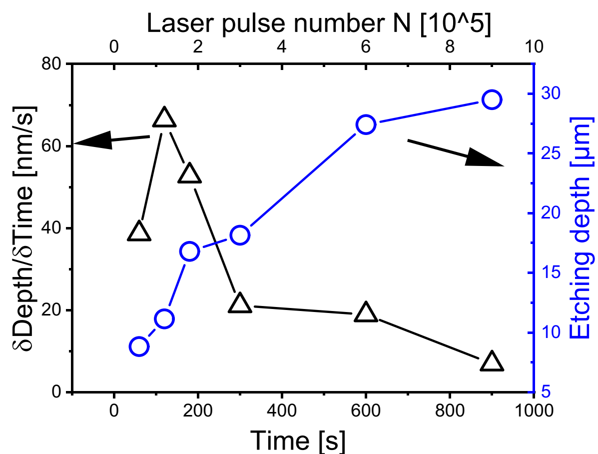

Fig. 4 Instantaneous etching rate (left scale) and etching depth (right scale) in dependency of the etch time (bottom scale) and laser pulse number (top scale). The plasma distance and the pulse energy were fixed at values of 100 μm and 740 μJ, respectively. The laser pulse number was caculated by considering the laser pulse repetion rate of $f_{rep.} = 1$ kHz. linies are for guiding the eyes

the instantaneous etching rate decreases with the increasing etch time from to a value of ~ 7 nm/ s at an etching time of 900 s as is seen in Fig. 4 too. Considering the pulse repetition rate $f_{rep.}$ of 1 kHz, an instantaneous etch depth per pulse can be calculated. The maximum is at an etching time of 120 s with a value for the instantaneous etch depth per pulse of ~ 0.07 nm/pulse that reduces finally to 0.007 nm/pulse. This found instantaneous etching rate per pulse is less than the value of the lattice plane separation for Ge [111] which is ~ 0.32 nm.

The dependence of etching depth on the plasma distance is shown in Fig. 5. The pulse energy and the etching time is fixed to 740 µJ and 180 s, respectively. It can be seen that the etching depth decreases nearly linearly with increasing plasma distance. Extrapolating the linear fit shown in Fig. 5, a maximum plasma distance of ~ 187 µm for achieving an etching can be calculated. In general, by decreasing the plasma distance, the etching depth increases. However, a very small plasma distance has been avoided to prevent direct laser irradiance and laser ablation.

The etching depth in dependence on the pulse energy is shown in Fig. 6. The etching time and plasma distance are fixed to values of 180 s and 100 µm, respectively. The etching depth increase with the pulse energy is monotone and almost linear. A linear fit of the experimental data is plotted in Fig. 6. The laser pulse energy threshold for etching can be estimated to be ~ 290 µJ by extrapolating the linear fit to the experimental data.

A top view of an exemplary etching grove is shown in Fig. 7. This etching groove was imaged by SEM. The edge of the etching grooves are rounded, and no steep features can be found, (therefore the contrast in the SEM image is low). The shape of the etching groove is oval and similar the shape of the laser induced plasma (see Fig. 2). All investigated etching grooves are rather smooth and show no surface features that can be attributed to laser ablation such as melting spheres, cracks, roughness, debris, LIPSS (laser induced periodic surface structures), as well as other redeposits. The center of the etching groove (marked with a with circle in Fig. 7), was investigated more in detail.

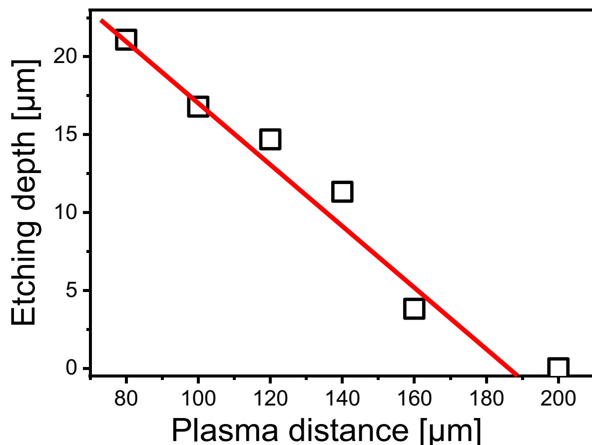

Fig. 5 Etch depth in dependence on the plasma distance. The etch time and pulse energy were fixed at value of 180 s and 740 µJ, respectively. The red line is a linear fit of the shown data

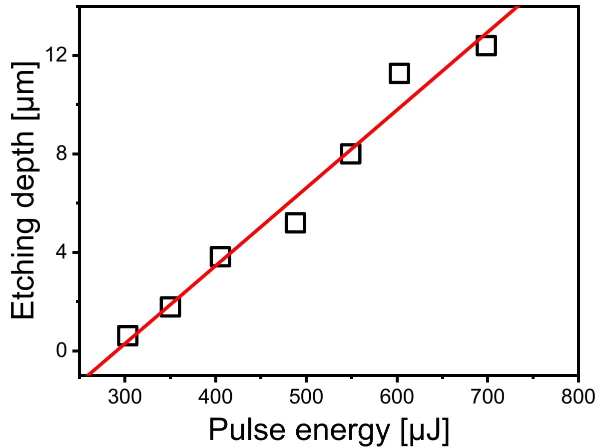

Fig. 6 Etching depth in dependency of the pulse energy. The plasma disatnce and the etching time were fixed at values of 100 μm and 180 s, respectively. The red line is a linear fit of the shown data

Figure 8a shows the surface (marked with a circle in Fig. 7) before the cleaning process and Fig. 8b shows the same area after the cleaning process. In the uncleaned area particles attached to the surface can be seen. These particles are completely removed due to the in the experimental detail section described cleaning process. By comparison the uncleaned and cleaned area no features were found in the cleaned surface which indicate that the particles (see Fig. 8a) provide a local masking effect during the etching process.

The AFM analysis of the area marked in Fig. 7 is shown in Fig. 9a. The AFM analysis was performed after the cleaning process. In the image it can be seen that the surface is covered with small dot like structures. The size of these dots is approximately 200 nm and the height are < 10 nm. Apart from these dot structures, the surface of the etching groove is defect free. Especially, the area between the strangled dots has a very low surface roughness. The surface roughness including the

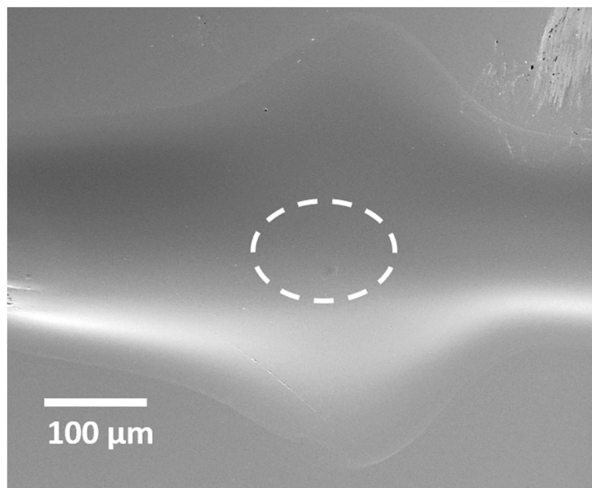

Fig. 7 SEM images of an etching groove. The etching time was 180 s, the pulse energy was 700 μJ and the plasma distance was 100 μm, respectively

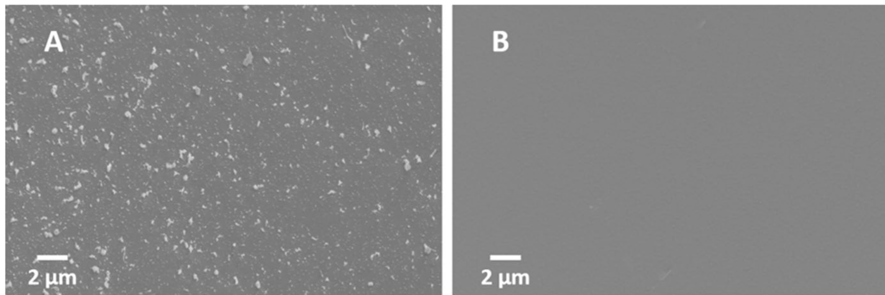

Fig. 8 SEM images of the central part of the etching groove marked in Fig. 7. In image **A** the surface is shown without the cleaning process described in the experimental detail section. In image **B** the same surface is shown after the cleaning process

dot patterns calculated from the measured area (10 µm x 10 µm) is ~ 2.4 nm rms. An AFM analysis of an unprocessed reference sample area is shown in Fig. 9b. The roughness of an untreated surface of the sample was ~ 1.5 nm rms (measured area of 10 µm x 10 µm).

In order to investigate the near-surface material composition TOF–SIMS analyses of sample before and after the etching process were performed. In Fig. 10a depth profiles of selected ion masses of an untreated reference sample without thermal or laser – plasma processing, an example etch groove, and the peripheral area are shown in comparison. The location of the measured areas is depicted in the optical microscopy image in Fig. 10b. The SIMS analysis field is situated in a rather shallow area near the etching groove center. An oxide surface layer is found in all measurements. A considerable amount of hydrogen is found within the oxide (Fig. 8a). However, hydrogen is detected inside the bulk germanium material as well. It is not clear, if the increased hydrogen level in the oxide is a pure increase in ionization probability due to the matrix effect or if an actual hydrogen accumulation is

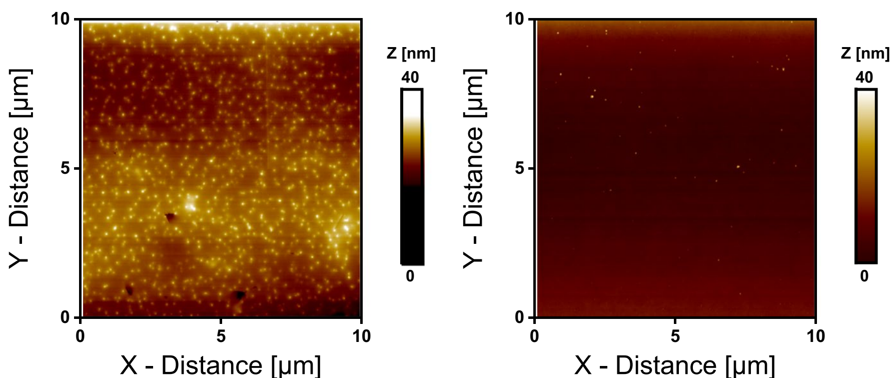

Fig. 9 (Right) AFM image of the central part of an etching groove which is marked with an circle in a. The height plot of the etched area showned some randomly distribute dots with a size of ~ 200 nm and a height of ~ < 10 nm. The calculate roughness after subtracting a fitted sphere is ~ 2.4 nm rms. (Left) AFM image of an unprocessed reference sample

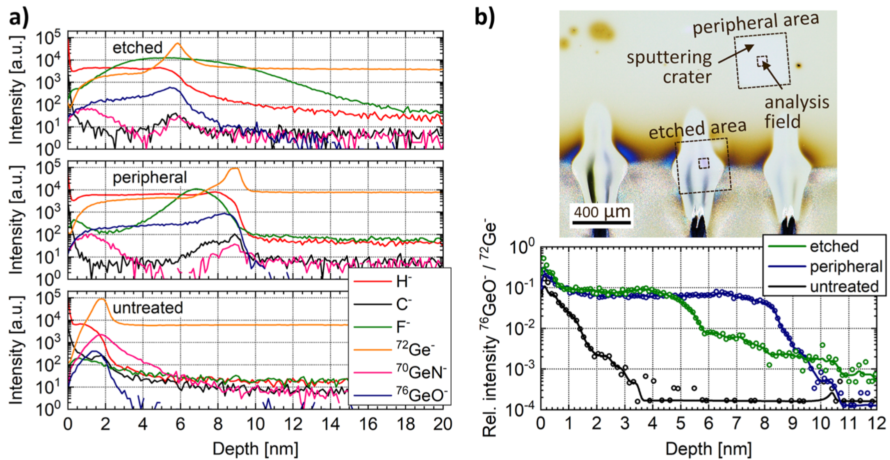

Fig. 10 **a** TOF–SIMS depth profiles measured in the etch groove region and the peripheral sample area. For comparison an untreated Ge (111) substrate is measured as a reference corresponding to the state before laser – plasma processing. **b** Optical microscopy image (bright-field view) of the analyzed sample areas and the relative intensity depth profiles of the $^{76}GeO^-$ / $^{72}Ge^-$ intensity ratio

present in the oxide layer. Nitric and carbon fractions are especially concentrated at the sample surface and drop quickly within the first nanometers in the oxide to a negligible level. Buried fractions of elemental fluorine are detected in the etching groove as well as the peripheral area. Note, during dynamic SIMS with cesium ions fluorine exhibits an increased secondary ion yield and its SIMS signal is typically one or more orders of magnitude higher than the matrix material signal. The fluorine concentration is maximum near the oxide/germanium interface. This situation is observed in the etching groove, but in the peripheral area as well. Thus, reactive fluorine species seem not to be located to the laser – plasma spot area only, but also in its surrounding. The fluorine incorporation into the sample surface seems to be thermally driven. An enhanced thermal impact can be expected due to the laser – plasma / surface interaction resulting in the observed, increased diffusive depth profile for fluorine, but hydrogen and oxygen as well. In contrast to the oxide/germanium interface, the sample surface is depleted of fluorine, probably due to fluorine consumption in the formation of volatile GeO_xF_y compounds at the surface. The direct verification of binary fragments consisting of germanium and fluorine by SIMS is difficult. The spectral position of $^{72}GeF^-$ is equal to $^{74}GeOH^-$ and except for $^{76}GeF^-$ the binary species for all germanium isotopes with fluorine are overlaid by a germanium hydroxide. However, for $^{76}GeF^-$ no hydroxide counterpart is apparent. In all measurements only negligible $^{76}GeF^-$ signal intensities are found within the depth profiles. This result indicates that the overall fluorine concentrations are very low inside the material. The high elemental fluorine count rates in Fig. 10 overestimate the fluorine content due to the high secondary ion yield of fluorine.

In the plot in Fig. 10b the $^{76}GeO^-$ / $^{72}Ge^-$ intensity ratio is shown in order to reduce the impact of varying ionization yields in the depth profiles, which especially

cause the increase of all signal intensities at the oxide to germanium interface. As a measure for the surface oxide thickness the depth value at 10% of the level intensity in the oxide layer is taken. On the untreated reference sample surface, the oxide layer determined by SIMS (Fig. 8b) is ~ 1.4 nm. A sharp transition between the oxide surface layer and the underlying bulk Ge is observed. Within ~ 3 nm the oxide drops to a negligible level. The same sharp transition is also obtained in the peripheral area after the laser – plasma etching, despite the oxide thickness is much increased to ~ 8.6 nm. In the etching groove an oxide layer with a thickness value of ~ 5.8 nm can be found. As mentioned above, in the interface between oxide layer and the bulk Ge an accumulation of fluorine is apparent. The fluorine as well as oxygen species drops are shallower than in the untreated surface and the peripheral area. Increased signals up to a depth of ~ 18 nm are found, indicating a higher local temperature and thus enhanced diffusion in the etch spot location during laser – plasma processing.

In order to investigate the surface modifications that are generated as by-products during the etching process, an XPS analysis of an exemplary etching groove has been performed and compared with an untreated reference area on the same sample, which was situated specifically far from the etched surface areas. Fluorine has two photoelectron peaks corresponding to binding energies of 685 eV (F 1 s) and 29 eV (F 2 s). In both sample areas no fluorine signal could be detected indicating that almost marginal fluorine amounts below the XPS detection limit < 0.1 at% are incorporated inside the oxide layer and in the germanium material below. Note, the circumstance that fluorine is detected in the TOF–SIMS experiments is related to a much higher sensitivity for fluorine and an increased detection range over five orders of magnitude. This further implies that no layer of fluorocarbons has been deposited on the surface due to the etching. In the untreated sample area, photoemission signals of Si and C can be found, which indicates the presence of small quantities of Si and C (Table 1). In contrast, Si signals cannot be found in the spectra of the etched surface. Moreover, the C amount is reduced in the etched surface. The spectra of Ge 3d are shown in Fig. 11. By comparing the spectra measured in the untreated area and the etched surface, a clear alternation of the Ge 3d core level footprint can be seen. In the peripheral area, four peaks at 33.1 eV (Ge^{4+}), 30.9 eV (Ge^{2+}), 29.9 eV (Ge^{1+}), and 29.4 eV (Ge^{0}) can be distinguished. Those values correspond well with published value [24, 25]. The main signal peak at 33.1 eV corresponds to Ge^{4+} bound in GeO_2. The Ge^{2+} and Ge^{1+} signals indicate the minor formation of suboxide species (GeO, Ge_2O) and the germanium matrix material is related to Ge^{0}

Table 1 Sample stoichiometry determined by XPS in the etching groove and the untreated sample area. Note, the difference in absolute composition values for both sample areas, if the Ge 3d peak (1st line) or the Ge $2p_{3/2}$ peak (2nd line) is used for the calculation

Sample area	Ge	O	C	Si
Etching groove	31.5 at% (Ge 3d)	61.1 at%	7.4 at%	–
	28.0 at% (Ge $2p_{3/2}$)	64.3 at%	7.7 at%	–
Untreated area	27.9 at% (Ge 3d)	55.6 at%	9.7 at%	6.8 at%
	24.0 at% (Ge $2p_{3/2}$)	58.6 at%	10.3 at%	7.1 at%

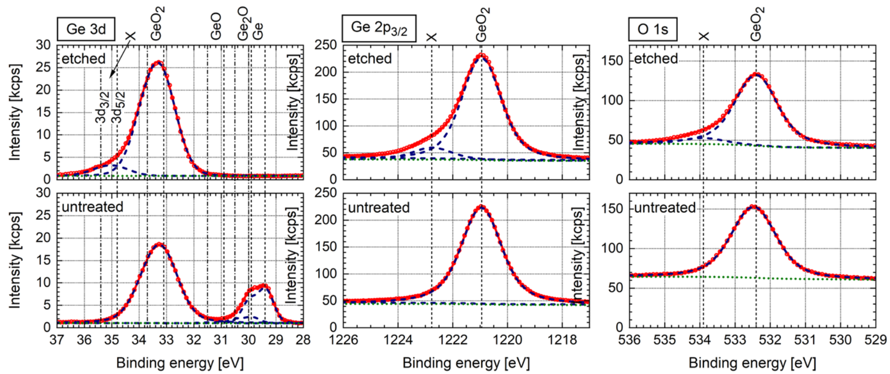

Fig. 11 XPS spectra for Ge 3d, Ge $2p_{3/2}$, and O 1 s of the etched and the untreated Ge surface

at 29.4 eV. In the spectra of the etched sample area every Ge atom is bound in GeO_2 and neither matrix Ge nor other bound Ge (such as GeO) can be found.

In Fig. 11 also the Ge $2p_{3/2}$ spectra for the untreated and etched sample areas are shown. Analysis of the Ge $2p_{3/2}$ core level signal shows in both sample areas that the Ge is fully bound in GeO_2. According to the different kinetic energies of the mean escape depth of photoelectrons is for the Ge $2p_{3/2}$ core level (0.9 ± 0.1 nm) less than that for the Ge 3d core level with (3.0 ± 0.3) nm [26]. Hence, in the etched area, where Ge $2p_{3/2}$ and Ge 3d appear both, as pure GeO_2 signals, the oxide thickness can be expected to be larger than 3.0 nm. This result corresponds well to the oxide thickness of 5.8 nm that was measured in SIMS. The Ge $2p_{3/2}$ of the unetched sample area is related only to Ge bound in GeO_2, but the Ge 3d feature shows contributions of suboxides and matrix Ge. This result implies a thin oxide layer with a thickness between 0.9 nm and 3.0 nm on the reference sample. In fact, the SIMS studies show an oxide layer thickness of 1.4 nm at the reference substrate area, which is in good accordance with literature values [27].

The main O 1 s peak for the etched and unetched surface areas is located at 532.4 eV (Fig. 11) that is addressable to GeO_2. Because the kinetic energy of the O 1 s photoelectrons is considerably lower than that of Ge 3d the escape depth is expected to be within the oxide layer, also in the untreated sample area. Note, at the high energy side of all XPS spectra of the etch groove area in Fig. 11 is a minor peak with a separation energy difference of ~ 1.7 eV to the main peaks appears, which is assumed to result from local sample charging and is thus ignored.

Table 1 summarizes the sample compositions determined by XPS. Different concentration values are found for using the Ge 3d peak (1st line) or the Ge $2p_{3/2}$ peak (2nd line) for composition calculation, which is attributed to the varying contributions of GeO_2, suboxides, and metallic germanium to the respective Ge core-level signal.

Discussion

The smooth, low defect surface morphology, as shown in Figs. 3 and 7, exclude laser ablation processes. Hence, the reactive micro plasma induced by optical breakdown in a CF_4/O_2 atmosphere at atmospheric pressure is responsible for Ge etching at a sample temperature of ~ 473 C°. The chemical activity of CF_4 is low at least up to 1000 K [28] and no thermal-activated etching of the Ge surface by CF_4 can be expected. Oxygen, however, as part of the etching gas, can interact with the germanium surface at these temperatures and resulting in a thermal-enhanced surface oxidation also of those areas not exposed to the laser-induced plasma. However, the local heat impact by LIP can increase Ge surface temperature additionally and enhance local surface oxidation. This conclusion is in accordance with the SIMS results of the peripheral surface area, where a higher oxide thickness of 8.6 nm is observed in comparison to a pristine surface which had an oxide thickness of 1.4 nm. In general, the laser-induced plasma must provide conditions, in particular reactive species, enabling chemical etching processes instead of laser ablation.

It is well known that plasmas can be generated in CF_4/O_2 mixtures by electrical excitation and due to that activated chemical species are formed from CF_4 and O_2 in consequence of dissociation and ionization processes [29]. Reactive fluorine and fluorine compounds can be formed by several reactions in the plasma such as dissociation, ionization and attachment reactions [29]. Here, the laser-induced optical breakdown resulting in plasma development (see the plasma emission in Fig. 2), so that similar species found in electrical activated plasmas can be expected.

During interaction of the plasma including the generated reactive species (O_x, CF_y) with the germanium surface two kinds of chemical reactions can be expected:

1. Germanium oxide formation due to chemical reactions of reactive oxygen species at the elevated temperatures (in addition to thermal oxidation).
2. Volatile germanium fluoride and oxifluoride species are formed as a result of the reaction of reactive fluorine species with the germanium oxide and germanium at the interface between Ge and its oxide.

The chemical reactions that can be observed in a CF_4 ICP plasma at Ge etching are summarized by Kyu-Hwan Shim et al. [30]. In addition to chemical reactions the contribution of accelerated ions (stimulated by the plasma potential) to the surface chemistry and sputter effects needs to be considered for low pressure plasma etching processes. Electrical pumped plasmas may differ from plasmas generated by laser-induced optical breakdown, but similar fundamental chemical reactions can be expected. However, the different plasma temperatures, the different dynamic and therefore the different energies of the charged particles probably cause a different weighting of the specific reactions. Further, despite high energetic, charged particles that can be generated by the high energy laser pulse; with increasing laser pulse energy an even higher excitation (ion energies) can be expected in the primary LIP. Despite such high ion energies in the primary laser plasma (the optical breakdown

size is similar the laser focus region) sputter effects can be neglected as the main free path length is small in relation to the plasma distance.

The instantaneous etching rate and its time dependence can be limited by each step involved in the process: the species generation in the plasma, the transport of these species to the surface, the reaction speed(s), the desorption and the removal of the reaction products from the reaction zone. In this relation the current discussion is limited to those processes for that the experiments provide evidence.

As shown in the first experiment (see Fig. 4), the instantaneous etching rate decreases with increasing of the etching time. Several factors such as plasma distance, the actual surface temperature, reactive species dilution (species deactivation) and alteration of the surface composition can be responsible for such effects. One important factor can be attributed to geometrical consideration, i.e. the plasma distance. With increasing etching time, the etching groove and therefore the plasma distance increasing. This, however, has consequences to the transport of the reactive species, the deactivation of the species, the surface temperature, and the plasma-generated radiation impact; all parameters affecting the reaction speed at the surface.

Another reason can be expected in the loading effects usually found at low pressure dry etching [31, 32] that relays to increased consumption of the reactive species for larger surfaces. However, the areal rise of the etching groove size can also not explain the instantaneous etching rate reduction so that loading effects cannot account alone for the observed effect. This area rise of the etching groove size in combination with the decreasing of the instantaneous etching rate can be linked to the fact that that the etching is in competition with a simultaneous oxidation of the germanium surface. By assuming that the surface oxidation is more pronounced with longer etching times and the that the material removal process based on oxidation is slower. The decrease of the etching with increasing of the plasma distance as depicted in Fig. 5 can be related to the following factors:

I) in contrast to other plasma based etching techniques the plasma source which is generated by the laser induced optical breakdown is limited in size and can be considered as a point/line source. As a result, the quantity of reactive species per unit area which can interact with the surface decreases with increase of the plasma distance. However, by this geometrical consideration a non-linear characteristic of the etching depth slope could be expected which is not seen experimentally. Therefore, other factors need to be considered.

II) The species that are generated have to be transported from their point of origin to the surface for successful etching. Because of the nearly atmospheric gas pressure, the mean free path is approximately ~ 100 nm and the main transport mechanism is supposed to be diffusion. Considering the mean free path length and the plasma distance the impact of collision becomes obvious. Therefore, a significant amount of reactive species can collide and interact with other reactive or neutral species. Due to this, some of the reactive species can be consumed by side reactions or can suffer from deactivation processes. The probability of these processes increases with increasing of the plasma distance.

The linear increase of the etching depth with increasing the laser pulse energy shown in Fig. 6 is unusual in particular in relation to standard laser ablation processes. However, such a linear etching behavior has been found in laser-induced backside etching [33, 34].

However, this linear characteristic may be a result of a synergetic, cumulative effect of multiple factors which influence the etching process. One of the factors is the increasing size/volume of the plasma with increasing pulse energy. Because of the increased plasma volume and the higher excitation, more reactive species can be formed. With increase of the plasma size, the plasma surface distance is reduced which increases the etching depth/rate according Fig. 5. With higher pulse energy a shift in the energy distribution function towards higher energy can be expected that can result in more ionization and longer decay times of excided species.

Besides these geometrical considerations, surface modifications during the etching process can account for the reduction of the etching rate. With the XPS analysis, it has been shown that after etching no significant fluorocarbon could found at the surface. However, it cannot be excluded that CF_x which is deposited during the etching is consumed by subsidiary reaction as proposed by Kim et al. [35] for Ge etching with inductively coupled plasma (ICP) CF_4/O_2 plasmas. Further, high concentration of atomic, ionized, or excided oxygen near surface can be expected due to the high O_2 concentration in the etching gas. This results also in an oxidation of possible deposited fluorocarbons. In consequence, since CF_x is part of the chemical reaction chain and may cover the surface in parts within the etching process and CF_x cannot be detected ex-situ after the etching process the oxidation of carbon/fluorocarbon seem a reasonable process step.

The XPS and SIMS results suggest that after the LIP-process no elemental Ge is near the surface, but the surface is covered with a GeO_x/GeO_xF_y layer with a thickness of approximated ~ 6 nm (see Fig. 11 and Table 1). Such oxide or oxifluoride layers can influence the etching mechanism and therefore the observed instantaneous etching rate. For instance, at plasma etching of Si with fluorine [16, 36] in an O_2 rich atmosphere, a passivation layer of SiO_xF_y layer is formed with higher oxygen concentration of the etching gas until a point where the oxyfluoride layer can block the etching almost completely [16, 36]. The oxide layer formation at Ge etching already at rather low oxygen contents can be understood with the higher affinity of Ge towards to oxygen compared to silicon [37]. As germanium has a high oxygen affinity and oxygen (GeO_xF_y) remains at the surface also for low oxygen contents but it was concluded that this GeO_xF_y layer does not inhibit the etching significantly [16, 36]. Further, the final Ge etching product for SF_6/O_2 etching gas mixtures is, however, GeF_4 [16]. The similarities of the measured and published XPS spectra suggest that the basic etching mechanism is similar despite different process parameters (pressure, gas composition) are used. It can be speculated that here, using CF_4 as a fluorine source, the oxygen can serve as an oxidant of the carbon forming CO_x molecules as the carbon amount at the surface after etching is low. The slightly increase of the surface roughness observed here (see Fig. 9a) can be credited the precipitates that maybe results from sample defects (residues from the polishing) or agglomeration of non-volatile retching residues. In comparison to low pressure dry etching observations (ICP of Ge)

where roughness related to sputter effects [30] and masking by carbon products [30] has been observed, here the roughness is not affected from such effects. this confirm previously discussed issues of a low energy of etching species and carbon oxidation at LIP CF_4/O_2 etching of Ge.

It is clear that other processes can contribute to the Ge etching. For instance the UV and X-ray radiation from the LIP [38–40] can be assumed to contribute to the etching process at all.

Conclusions

High quality machining by dry etching of crystalline (111) Ge with an optically pumped CF_4/O_2 plasma has been demonstrated. The laser micro plasma has been generated by an optical breakdown in a CF_4/O_2 gas mixture near atmospheric pressure (absolute pressure: 850 ± 50 mBar) by focusing laser pulses having a pulse duration of 150 fs with a 60 mm lens. After exceeding a threshold pulse energy for plasma formation an etching of the Ge can be observed. The etching depth increase with increasing laser pulse energy. The average absolute etching depth per laser pulse of less than 0.03 nm/pulse underline the accuracy of the etching that is below the lattice constant of Ge (~0.56 nm). In addition, the surface of the etching grooves is smooth with a roughness of <2.4 nm rms and no signs of melting or cracking has been found. The observed decrease of the instantaneous etching rate with time is probably related to the increased plasma surface distance (etching depth), higher surface area and the formation of a GeO_2 layer, which has been detected by XPS. Otherwise, the surface is chemically clean without any attachments of fluoropolymers. This presents laser-based dry etching process as an ultrahigh precision machining tool due to the very low instantaneous etching rate per laser pulse and better surface quality in particular in comparison to laser ablation processes. Further, in comparison with other plasma etching techniques, e.g. ICP, the etching quality is similar, but no vacuum is required. The small footprint of this etching tool enables direct laser scribing with optical quality. Therefore, this laser etching process can provide new processing capabilities such as the generation of free form optics or correction of optical waviness for Ge infrared optical devices.

Acknowledgements The authors wish to acknowledge the help of Ms. I. Mauersberger with the SEM and AFM measurements. The datasets generated during and/or analysed during the current study are available from the corresponding author on reasonable request. Further, the work was funded by the Deutsche Forschungsgemeinschaft (DFG, German Research Foundation) – No. 392226212.

Funding Open Access funding enabled and organized by Projekt DEAL.

Open Access This article is licensed under a Creative Commons Attribution 4.0 International License, which permits use, sharing, adaptation, distribution and reproduction in any medium or format, as long as you give appropriate credit to the original author(s) and the source, provide a link to the Creative Commons licence, and indicate if changes were made. The images or other third party material in this article are included in the article's Creative Commons licence, unless indicated otherwise in a credit line to the material. If material is not included in the article's Creative Commons licence and your intended use is not permitted by statutory regulation or exceeds the permitted use, you will need to obtain permission

directly from the copyright holder. To view a copy of this licence, visit http://creativecommons.org/licenses/by/4.0/.

References

1. Lee, R.E.: Microfabrication by ion-beam etching. J. Vac. Sci. Technol. **16**, 164–170 (1979)
2. Cuomo, J.J., Rossnagel, S.M., Haufman, H., Komanduri, R.: Handbook of ion beam processing technology: principles, deposition, film modification, and synthesis (1990)
3. Shul, R.J., Pearton, S.J.: Handbook of advanced plasma processing techniques, Springer Science & Business Media (2011)
4. Cardinaud, C., Peignon, M.-C., Tessier, P.-Y.: Plasma etching: principles, mechanisms, application to micro-and nano-technologies. Appl. Surf. Sci. **164**, 72–83 (2000)
5. Nojiri, K.: Dry etching technology for semiconductors, Springer (2015)
6. Arnold, T., Boehm, G., Schindler, A.: Ultrahigh-rate plasma jet chemical etching of silicon. J. Vac. Sci. Technol. A **19**, 2586–2589 (2001)
7. Eichentopf, I.M., Böhm, G., Meister, J., Arnold, T.: Reactive Plasma Jet High-Rate Etching of SiC. Plasma Process. Polym. **6**, S204–S208 (2009)
8. Paetzelt, H., Böhm, G., Arnold, T.: Etching of silicon surfaces using atmospheric plasma jets. Plasma Sources Sci. Technol. **24**, 025002 (2015)
9. Darnon, M., de Lafontaine, M., Volatier, M., Fafard, S., Arès, R., Jaouad, A., Aimez, V.: Deep germanium etching using time multiplexed plasma etching. J. Vac. Sci. Technol. B **33**, 060605 (2015)
10. Shim, K.-H., Yang, H.Y., Kil, Y.-H., Yang, H.D., Yang, J.-H., Hong, W.-K., Kang, S., Jeong, T.S., Kim, T.S.: Nanoscale dry etching of germanium by using inductively coupled CF 4 plasma. Electron. Mater. Lett. **8**, 423–428 (2012)
11. Shim, K., Kil, Y., Yang, H., Park, B., Yang, J., Kang, S., Jeong, T., Kim, T.S.: Characteristics of germanium dry etching using inductively coupled SF6 plasma. Mater. Sci. Semicond. Process. **15**, 364–370 (2012)
12. Oehrlein, G., Bestwick, T., Jones, P., Jaso, M., Lindström, J.: Selective dry etching of germanium with respect to silicon and vice versa. J. Electrochem. Soc. **138**, 1443 (1991)
13. McLane, G., Dubey, M., Wood, M., Lynch, K.: Dry etching of germanium in magnetron enhanced SF 6 plasmas. J. Vac. Sci. Technol., B: Microelectron. Nanometer Struct. Process. Meas. Phenom. **15**, 990–992 (1997)
14. Wongwanitwattana, C., Shah, V.A., Myronov, M., Parker, E.H., Whall, T., Leadley, D.R.: Precision plasma etching of Si, Ge, and Ge: P by SF6 with added O2. J. Vac. Sci. Technol. A: Vac. Surf. Films **32**, 031302 (2014)
15. Campo, A., Cardinaud, C., Turban, G.: Investigation of Si and Ge etching mechanisms in radiofrequency CF2-O2 plasma based on surface reactivities. Plasma Sources Sci. Technol. **4**, 398 (1995)
16. Campo, A., Cardinaud, C., Turban, G.: Comparison of etching processes of silicon and germanium in SF6–O2 radio-frequency plasma. J. Vac. Sci. Technol. B: Microelectron. Nanometer Struct. Process. Meas. Phenom. **13**, 235–241 (1995)
17. Nath, A.: Laser etching and dry processing. Bull. Mater. Sci. **11**, 159–166 (1988)
18. Bäuerle, D.: Laser processing and chemistry, Springer Science & Business Media (2013)
19. Kullmer, R., Bäuerle, D.: Laser-induced chemical etching of silicon in chlorine atmosphere. Appl. Phys. A **43**, 227–232 (1987)
20. Baklanov, M., Beterov, I., Repinskii, S., Rzhanov, A., Chebotaev, V., Yurshina, N.: Initiation of a surface chemical reaction between single-crystal germanium and bromine gas by using a powerful argon laser, in: Soviet Physics Doklady pp. 312. (1974)
21. Affrossman, S., Bailey, R., Cramer, C., Cruickshank, F., Macallister, J., Alderman, J.: Laser photochemical etching of silicon. Appl. Phys. A **49**, 533–542 (1989)
22. Elhadj, S., Guss, G., Matthews, M.J., Bass, I.: Laser-induced gas plasma etching of fused silica under ambient conditions, in: Laser-Induced Damage in Optical Materials: 2012, International Society for Optics and Photonics pp. 853022. (2012)
23. Ehrhardt, M., Lorenz, P., Han, B., Zimmer, K.: Laser-induced reactive microplasma for etching of fused silica. Appl. Phys. A **126**, 842 (2020)

24. Prabhakaran, K., Ogino, T.: Oxidation of Ge (100) and Ge (111) surfaces: an UPS and XPS study. Surf. Sci. **325**, 263–271 (1995)
25. Schmeisser, D., Schnell, R., Bogen, A., Himpsel, F., Rieger, D., Landgren, G., Morar, J.: Surface oxidation states of germanium. Surf. Sci. **172**, 455–465 (1986)
26. Deegan, T., Hughes, G.: An X-ray photoelectron spectroscopy study of the HF etching of native oxides on Ge (111) and Ge (100) surfaces. Appl. Surf. Sci. **123**, 66–70 (1998)
27. Sahari, S.K., Murakami, H., Fujioka, T., Bando, T., Ohta, A., Makihara, K., Higashi, S., Miyazaki, S.: Native oxidation growth on Ge (111) and (100) surfaces. Jpn. J. Appl. Phys. 50 (2011) 04DA12
28. Sun, J.-W., Park, D.-W.: CF4 decomposition by thermal plasma processing. Korean J. Chem. Eng. **20**, 476–481 (2003)
29. Fridman, A.: Plasma chemistry, Cambridge university press (2008)
30. Shim, K.-H., Yang, H.Y., Kil, Y.-H., Yang, H.D., Yang, J.-H., Hong, W.-K., Kang, S., Jeong, T.S., Kim, T.S.: Nanoscale dry etching of germanium by using inductively coupled CF4 plasma. Electron. Mater. Lett. **8**, 423–428 (2012)
31. Mogab, C.: The loading effect in plasma etching. J. Electrochem. Soc. **124**, 1262 (1977)
32. Choi, D.-Y., Kim, N.-H., Kim, S.-Y.: Reduction of loading effects with the sufficient vertical profile for deep trench silicon etching by using decoupled plasma sources. J. Mater. Process. Technol. **209**, 5818–5829 (2009)
33. Böhme, R., Braun, A., Zimmer, K.: Backside etching of UV-transparent materials at the interface to liquids. Appl. Surf. Sci. **186**, 276–281 (2002)
34. Zimmer, K., Ehrhardt, M., Böhme, R.: Laser-Induced Backside Wet Etching: Processes, Results, and Applications, in: G. Yang (Ed.) Laser Ablation in Liquids, Pan Stanford Publishing Singapore pp. 1013–1132 (2012)
35. Kim, T.S., Choi, S.-S., Im Shin, M., Jeong, T.S., Kang, S., Choi, C.-J., Shim, K.-H.: Dry etching of germanium using inductively coupled Ar/CCl 2 F 2/Cl 2 plasma. Electron. Mater. Lett. **6**, 35–39 (2010)
36. Cardinaud, C., Campo, A.G.: Turban, Surface Reactivity of Silicon and Germanium in CF 4-O 2 Reactive Ion Etching, MRS Online Proceedings Library Archive, **324**, (1993)
37. Tong, Q.Y., Gutjahr, K., Hopfe, S., Gösele, U., Lee, T.H.: Layer splitting process in hydrogen-implanted Si, Ge, SiC, and diamond substrates. Appl. Phys. Lett. **70**, 1390–1392 (1997)
38. Diels, J.-C., Rudolph, W.: Ultrashort laser pulse phenomena, Elsevier (2006)
39. Von der Linde, D., Schüler, H.: Breakdown threshold and plasma formation in femtosecond laser–solid interaction. JOSA B **13**, 216–222 (1996)
40. Lamour, E., Prigent, C., Rozet, J.-P., Vernhet, D.: X-ray production in short laser pulse interaction with rare gas clusters, in: Journal of Physics: Conference Series, IOP Publishing pp. 012035 (2007)

Publisher's Note Springer Nature remains neutral with regard to jurisdictional claims in published maps and institutional affiliations.